The Astrophysical Journal, 909:130 (11pp), 2021 March 10 https://doi.org/10.3847/1538-4357/abd946

Ultrafaint [C II] Emission in a Redshift = 2 Gravitationally Lensed Metal-poor Dwarf Galaxy

Matus Rybak[1], E. da Cunha[2,3], B. Groves[2,4], J. A. Hodge[1], M. Aravena[5], M. Maseda[1], L. Boogaard[1], D. Berg[6], S. Charlot[7], R. Decarli[8], D. K. Erb[9], E. Nelson[10], C. Pacifici[11], K. B. Schmidt[12], F. Walter[13,14], and A. van der Wel[13,15]

[1] Leiden Observatory, Niels Bohrweg 2, 2333CA Leiden, The Netherlands; mrybak@strw.leidenuniv.nl
[2] International Centre for Radio Astronomy Research (ICRAR), University of Western Australia, 35 Stirling Highway, Crawley, WA 6009, Australia
[3] ARC Centre of Excellence for All Sky Astrophysics in 3 Dimensions (ASTRO 3D), Australia
[4] Research School of Astronomy and Astrophysics, Australian National University, Canberra, ACT 2611, Australia
[5] Núcleo de Astronomía, Facultad de Ingeniería y Ciencias, Universidad Diego Portales, Av. Ejército 441, Santiago, Chile
[6] Department of Astronomy, The University of Texas at Austin, 2515 Speedway Boulevard Stop C1400, Austin, TX 78712, USA
[7] Sorbonne Université, UPMC-CNRS, UMR7095, Institut d'Astrophysique de Paris, F-75014, Paris, France
[8] INAF—Osservatorio di Astrofisica e Scienza dello Spazio, via Gobetti 93/3, I-40129, Bologna, Italy
[9] The Leonard E. Parker Center for Gravitation, Cosmology and Astrophysics, Department of Physics, University of Wisconsin-Milwaukee, 3135 N. Maryland Avenue, Milwaukee, WI 53211, USA
[10] Department of Astrophysical and Planetary Sciences, University of Colorado, Boulder, CO 80309, USA
[11] Space Telescope Science Institute, 3700 San Martin Drive, Baltimore, MD 21218, USA
[12] Leibniz-Institut für Astrophysik Potsdam (AIP), An der Sternwarte 16, D-14482 Potsdam, Germany
[13] Max-Planck Institut für Astronomie, Königstuhl 17, D-69117, Heidelberg, Germany
[14] National Radio Astronomy Observatory, Pete V. Domenici Array Science Center, P.O. Box O, Socorro, NM 87801, USA
[15] Sterrenkundig Observatorium, Department of Physics and Astronomy, Ghent University, Belgium
Received 2020 September 13; revised 2021 January 4; accepted 2021 January 5; published 2021 March 11

Abstract

Extreme emission-line galaxies (EELGs) at redshift $z = 1-2$ provide a unique view of metal-poor, starburst sources that are the likely drivers of the cosmic reionization at $z \geqslant 6$. However, the molecular gas reservoirs of EELGs—the fuel for their intense star formation—remain beyond the reach of current facilities. We present ALMA [C II] and PdBI CO(2–1) observations of the $z = 1.8$, strongly lensed EELG SL2S 0217, a bright Lyα emitter with a metallicity $0.05\,Z_{\odot}$. We obtain a tentative ($\sim 3\sigma$–4σ) detection of the [C II] line and set an upper limit on the [C II]/SFR (star-forming rate) ratio of $\leqslant 1 \times 10^6\,L_{\odot}/(M_{\odot}\ \mathrm{yr}^{-1})$, based on the synthesized images and visibility-plane analysis. The CO(2–1) emission is not detected. Photoionization modeling indicates that up to 80% of the [C II] emission originates from neutral or molecular gas, although we cannot rule out that the gas is fully ionized. The very faint [C II] emission is in line with both nearby metal-poor dwarfs and high-redshift Lyα emitters, and predictions from hydrodynamical simulations. However, the [C II] line is 30× fainter than predicted by the De Looze et al. [C II]–SFR relation for local dwarfs, illustrating the danger of extrapolating locally calibrated relations to high-redshift, metal-poor galaxies.

Unified Astronomy Thesaurus concepts: Dwarf galaxies (416); Lyman-alpha galaxies (978); Gravitational lensing (670); High-redshift galaxies (734); Submillimeter astronomy (1647)

1. Introduction

The Epoch of Reionization (EoR) is one of the main frontiers of present-day astrophysics. Recent results suggest that the reionization is likely driven by low-metallicity dwarf ($M_{\star} \lesssim 10^9\,M_{\odot}$) galaxies with intense star formation rates; due to their low gas and dust content, a large fraction of UV photons will be able to escape and reionize the neutral intergalactic medium (e.g., Robertson et al. 2010, 2015; Atek et al. 2015; Stark 2016). These metal-poor dwarf galaxies contribute significantly to the cosmic star-forming rate (SFR) at $z \geqslant 3$ (e.g., Bouwens et al. 2009). Consequently, characterizing the star-forming processes in $z \geqslant 6$ dwarf galaxies presents a crucial step toward understanding the evolution of galaxies at early cosmic times. However, these faint, high-redshift dwarf galaxies remain elusive due to the limitations of current facilities (mainly the Hubble Space Telescope and the Spitzer Space Telescope), along with the fact that for the most distant targets, the diagnostic-rich optical emission is shifted to the near-IR regime and thus currently unobservable—a situation that will be soon remedied by the James Webb Space Telescope. Consequently, large uncertainties remain on the physical mechanisms of galaxy-led reionization, such as the actual fraction of ionizing photons that escape their interstellar medium (ISM), their star formation efficiency, and feedback processes at play.

An alternative to studying directly the $z \geqslant 6$ dwarf galaxies is to target the intermediate-redshift ($z \sim 2$) extreme emission-line galaxies (EELGs; Atek et al. 2011; van der Wel et al. 2011; Maseda et al. 2013, 2014; Amorín et al. 2015), which are likely analogs of primordial galaxies at the EoR and can be studied much more efficiently, particularly in emission and absorption lines. EELGs have been identified through extremely high equivalent widths (EWs) of optical emission lines such as [O III] 5007 Å (with rest-frame EW exceeding 500 Å), via excess emission in HST/WFC3 broadband filters (van der Wel et al. 2011), and through HST/WFC3 grism spectroscopy (Maseda et al. 2018). Spectroscopic and photometric follow-up confirm that these are low-mass ($M_{\star} \sim 10^8$–$10^9\,M_{\odot}$), low-metallicity ($Z < 0.30\,Z_{\odot}$) dwarf galaxies with high SFRs ($\sim$10–100 $M_{\odot}\mathrm{yr}^{-1}$), likely undergoing an intense but short-

lived burst of star formation (e.g., Maseda et al. 2013, 2014; Masters et al. 2014; Tang et al. 2019).

While rest-frame UV and optical studies of high-redshift star-forming dwarfs have primarily targeted the ionized ISM, their intense star formation must be fueled by cold neutral gas. In particular, measuring the cold gas reservoirs of high-redshift dwarfs is crucial for understanding the timescales on which their high-mass star formation can be maintained. However, direct observations of the cold ISM phase in these faint, metal-poor sources are extremely challenging, even at $z \sim 1$–2.

Our best bet for probing the molecular gas content of these metal-poor galaxies is the [C II] 158 μm line, thanks to its low critical density and large intrinsic brightness. At $z \sim 2$, Herschel and ALMA Band 9 [C II] observations have been instrumental in probing the gas content of $M_\star = 10^9$–10^{11} $M_\odot$ galaxies (e.g., Stacey et al. 2010; Brisbin et al. 2015; Schaerer et al. 2015; Zanella et al. 2018). Crucially, for the EoR sources, the [C II] line is easily observable with ALMA and has become the chief probe of cool gas in early galaxies (e.g., Maiolino et al. 2005, 2015; Knudsen et al. 2016; Bradač et al. 2017; Matthee et al. 2019; see Hodge & da Cunha 2020 for a recent review). At the same time, the [C II] emission in high-redshift galaxies has been explored by a number of cosmological (e.g., Olsen et al. 2017; Lagache et al. 2018) and zoom-in simulations (e.g., Vallini et al. 2015; Katz et al. 2017; Pallottini et al. 2019; Lupi & Bovino 2020).

In this paper, we attempt to study the neutral ISM in the strongly gravitationally lensed, $z \sim 2$ SL2S 021737–051329 (henceforth SL2S 0217, J2000 02^h17^m $37\overset{s}{.}237$–$05^d13^m29\overset{s}{.}7$), targeting the [C II] line with the Atacama Large Millimeter/submillimeter Array (ALMA) and CO(2–1) with the Plateau de Bure Interferometer (PdBI). Thanks to its large magnification, SL2S 0217 provides a unique opportunity to detect the neutral ISM in a high-redshift EELG with a stellar mass of just 10^8 $M_\odot$—1 dex lower than any previous $z \sim 2$ study.

This paper is structured as follows: Section 2 presents our ALMA and PdBI observations, data combination, and imaging procedures; Section 3 presents the derivation of the source-plane upper limits on the [C II] and CO(2–1) luminosities. In Section 4, we compare our [C II] nondetection to the expectations from photoionization modeling (Section 4.1), various empirical and theoretical [C II]–SFR relationships (Section 4.2), as well as local and high-redshift observations (Section 4.3). Finally, we discuss the fate of the molecular gas in SL2S 0217 (Section 4.4) and the prospects of detecting the [C II] emission from SL2S 0217–like dwarfs in the EoR (Section 4.5).

2. Observations and Imaging

2.1. Target Description

SL2S 0217 is a redshift $z = 1.844$ EELG, strongly gravitationally lensed by a $z = 0.6459$ elliptical galaxy. SL2S 0217 was serendipitously discovered by Geach et al. (2007; source ID: SXDF-iS-170569). Thanks to its position under the cusp of the lensing caustic, SL2S 0217 is lensed into a brilliant, $2\overset{''}{.}5$ long Einstein arc, with a fainter counterimage. The lens system includes a second, doubly imaged background source, SL2S 0217.X, at $z = 2.29$ (Brammer et al. 2012).

The stellar content of SL2S 0217 was studied by Brammer et al. (2012, B12) using HST GRISM spectroscopy and Berg et al. (2018, B18) using Keck/LRIS optical spectroscopy.

Table 1
SL2S 0217: Intrinsic (Delensed) Properties Adapted from Berg et al. (2018, B18) and (2019, E19), with the [C II] and CO(2–1) Upper Limits Derived Assuming the $R \leqslant 3$ kpc Aperture from the $1''$ Taper Images (Figure 1) and a Magnification Factor $\mu = 16$

			Reference
$z_{\rm spec}$		1.844	B18
$M_\star$	$[M_\odot]$	$(1.8 \pm 0.4) \times 10^8$	B18
SFR	$[M_\odot\ {\rm yr}^{-1}]$	23 ± 2	B18
$\mu_{\rm UV}$		17.3 ± 1.2	B18
12+log(O/H)		7.5	B18
$R_{1/2}^{\rm UV}$	[kpc^2]	1.0×0.5	E19
$L_{\rm [C\ II]}$[a]	$[L_\odot]$	$\leqslant 2.1 \times 10^7$ (3.2σ)	Section 3.1
$L'_{\rm [C\ II]}$	[K km s^{-1} pc^2]	$\leqslant 1 \times 10^8$ (3.2σ)	Section 3.1
$S_{160\mu{\rm m}}$	mJy	$\leqslant 0.23$ (3σ)	Section 3.1
$L_{\rm CO(2-1)}$	$[L_\odot]$	$\leqslant 1.3 \times 10^5$ (3σ)	Section 3.1
$L'_{\rm CO(2-1)}$	[K km s^{-1} pc^2]	$\leqslant 4 \times 10^8$ (3σ)	Section 3.1
$M_{\rm H_2}^{\rm [C\ II]}$	$[M_\odot]$	$\leqslant 2.1 \times 10^9$	Section 4.4

Notes. For solar metallicity, we adopt the Asplund et al. (2009) value of 12 + log(O/H) = 8.69. The molecular gas mass $M_{\rm H_2}$ is derived from the [C II] luminosity using the Madden et al. (2020) conversion factor.
[a] Based on our tentative image-plane detection; see Figure 2.

Pixelated lens modeling of SL2S 0217 based on HST data[16] was performed by Cooray et al. (2011), B18, and Erb et al. (2019); in the B18 model, the HST F606W continuum is magnified by a factor of ∼17, with a source-plane UV half-light radius of ∼0.35 kpc. We adopt the source-plane properties listed in Table 1, based on the B18 lens model. The $Z = 0.05\ Z_\odot$ metallicity of SL2S 0217 is typical of $z \sim 6$ galaxies with the same stellar mass (see FIRSTLIGHT simulations; Langan et al. 2020), underlining its suitability as an EoR analog.

The spatial distribution of the Lyα emission in SL2S 0217 was studied by Erb et al. (2019, E19) using narrowband HST imaging. This revealed a 0.6 kpc offset between Lyα and the UV continuum, indicating a varying column density of neutral hydrogen across the source, with the bulk of the Lyα photons escaping along a low column-density channel. The long-wavelength spectral energy distribution of SL2S 0217 is only poorly sampled, with a single detection in the Spitzer/MIPS 24 μm imaging (B12; 7.3–9.1 μm rest frame, including the 7.7 and 8.6 μm polycyclic aromatic hydrocarbon (PAH) bands), which indicates significant hot-dust and/or PAH emission. In this paper, we extend this comprehensive data set to the far-infrared and millimeter-wave regime, targeting the [C II] 158 μm line.

We assume a flat ΛCDM cosmology, with $\Omega_m = 0.315$ and $H_0 = 67.4\ {\rm km\ s^{-1}\ Mpc^{-1}}$ (Planck Collaboration et al. 2020). At $z = 1.844$, this translates to a luminosity distance $D_L = 14460$ Mpc; $1''$ corresponds to a physical distance of 8.65 kpc (Wright 2006).

2.2. ALMA Band 9 Observations and Imaging

We combine deep ALMA Band 9 observations of the [C II] line ($f_0 = 1900.539$ GHz) and the underlying rest-frame 160 μm continuum from the ALMA projects #2016.1.00142.S and #2016.1.00776.S.

The ALMA program #2016.1.00142.S (PI: da Cunha) observations were carried out in two array configurations:

[16] See also Tu et al. (2009) and B12 for parametric lens models.

Table 2
ALMA Band 9 Synthesized Beam Size, Position Angle, and rms Sensitivity for the [C II] Line (measured at 668 GHz over 250 MHz bandwidth) and the Rest-frame 160 μm Continuum as a Function of (u, v) Taper

Taper	Beam FWHM (PA) (arcsec, deg)	σ ([C II]) (mJy beam^{-1})	σ (cont.) (mJy beam^{-}1)
Full res	0.26 × 0.23 (57)	1.28	0.23
0.″5	0.65 × 0.57 (−9)	1.44	0.29
1.″0	1.01 × 0.92 (−9)	1.91	0.44

C43-1 (2018 July 6) and C43-2 (2018 August 16). The baseline length ranged between 15 and 314 m (C43-1) and 15–479 m (C43-2). Forty 12 m antennas were used on both dates. The primary beam FWHM was 9.″0 at 680 GHz. The precipitable water vapor (pwv) ranged between 0.4 and 0.5 mm. The total observing time was 2.7 hr, with a total on-source time of 67 minutes.

The spectral setup consisted of four spectral windows (SPWs) with 480 channels of 3.906 MHz each, giving a total bandwidth of 2.0 GHz per SPW. The individual SPWs were centered at 667.61, 669.53, 649.91, and 648.03 GHz.

As the ALMA pipeline products suffered from calibration issues, we calibrated the data manually by completely flagging antennas with high system temperature: C43-1 configuration: DA62, DA44, DA50, DV09, DV24; C43-2: DA62. We used DV07 as the reference antenna due to its low system temperature, good bandpass stability, and central position in the array.

We supplemented these data by observations from the ALMA program #2016.1.00776.S (PI: Cooray). These were taken in two array configurations: C43-2 with forty-seven 12 m antennas (2018 October 19) and C43-6 with fifty-one 12 m antennas (2016 October 1 and 14). The baseline length ranged between 15 and 3145 m (C43-6) and baselines 15 and 484 m (C43-2), the pwv ranged between 0.55 and 0.80 mm. The on-source time was 47.0 minutes for each configuration. The spectral setup consisted of four SPWs configured with 128 15.625 MHz wide channels (2.0 GHz bandwidth per SPW), with central frequencies of 664.95, 666.64, 668.34, and 670.03 GHz. For the C43-6 configuration, we manually flagged antennas DA43, DV14, and DV17. This reduced the total number of antennas to 48.

For the imaging, we concatenate the visibilities from both ALMA programs to maximize the signal-to-noise ratio (S/N); the total on-source time is 160 minutes. For the C43-6 configuration, we discard all baselines longer than 1000 kλ, as adding the long baselines significantly reduces the surface brightness sensitivity of the combined data set. The resulting (u, v)-plane coverage provides sensitivity to spatial scales between 0.″21 and 6.″2; given the arc length of 2.″5, we do not expect any structure to be resolved out.

We produce dirty images of the concatenated data set using natural weighting, at the full angular resolution and using a 0.″5 and 1.″0 Gaussian taper. For the [C II] line, we create several dirty-image cubes using different (u, v)-plane tapers (no taper, 0.″5 and 1.″0 taper) and channel widths ($\Delta f = 50$–500 MHz, equivalent to 25–225 km s^{-1}). The $\sigma_{\rm rms}$ levels in the resulting images match the expected ALMA sensitivity within 10%.

For the continuum image, we combine all of the SPWs, flagging the channels affected by atmospheric lines. The resulting beam sizes and rms sensitivity for the [C II] and Band 9 continuum imaging are listed in Table 2. With a sensitivity of $\sigma_{\rm rms} = 1.3$ mJy/beam over 250 MHz bandwidth (3.7 mJy/beam over 10 km s^{-1}), the combined data set ranks among the deepest ALMA Band 9 observations to date.

Figure 1 presents the resulting synthesized images. We do not find any significant ($\geqslant 5\sigma$) [C II] or rest-frame 160 μm continuum emission. However, the [C II] images show a suggestive 2σ–3σ emission along the main Einstein arc (see discussion below). In addition, we obtain a tentative (2σ–4σ) detection of the rest-frame 140 μm continuum from the secondary lensed source SL2S 0217.X ($z = 2.29$; B12).

The ALMA data were reduced and imaged using the Common Astronomy Software Applications package (CASA; McMullin et al. 2007), versions 5.1 and 5.4.

2.3. PdBI Band 1 Observations and Imaging

In addition to the ALMA observations of the [C II] 158 μm line, we target the CO(2–1) line using the Plateau de Bure Interferometer (PdBI) with the WideX correlator (program X037, PI: Aravena). The PdBI data were taken between 2013 June 15 and 2013 September 14 in a total of 16 successful tracks. The total on-source time was 29.6 hr (five-antenna equivalent); the total observing time was 40 hr. All observations were carried out in the most compact D configuration, with five 15 m antennas. The baseline length ranged between 15 and 97 m, resulting in a synthesized beam FWHM = 7″; the source is thus completely unresolved. The observations covered a frequency range of 79.6–83.2 GHz with a spectral resolution of 2 MHz. The resulting rms sensitivity at the expected frequency of the CO(2–1) line is 0.28 mJy beam^{-1} over a 100 km s^{-1} bandwidth. The data were reduced using the GILDAS/CLIC package (http://www.iram.fr/IRAMFR/GILDAS).

3. Results

3.1. [C II] Line and 160 μm Continuum

3.1.1. Searching for Signal in the Image Plane

To convert the image-plane [C II] flux to source-plane (intrinsic) flux, we need to account for the gravitational lensing. The magnification of the extended source depends on its surface brightness distribution and the lensing geometry. Although we could simply assume that the [C II] emission is cospatial with the HST continuum, resolved observations of high-redshift galaxies have revealed kiloparsec-scale offsets between the rest-frame UV and [C II] emission (e.g., Maiolino et al. 2015; Carniani et al. 2017) and very extended [C II] reservoirs (e.g., Carniani et al. 2018; Matthee et al. 2019; Carniani et al. 2020). If [C II] is significantly offset from the UV continuum, the [C II] might be less magnified the UV, increasing the source-plane $L_{\rm [C\,II]}$ upper limit.

We consider three circular source-plane apertures centered on the UV-continuum peak, with a radius $R = 1.0$, 2.0, and 3.0 kpc; the latter is comparable to the largest [C II] reservoirs observed in (much more massive) $z \sim 6$ galaxies (Carniani et al. 2020). We project these into the sky plane using the Cooray et al. (2011) lens model for the lensing galaxy. To maximize the S/N, we consider only the part of the sky-plane aperture corresponding to the main arc (Figure 1); as the arc accounts for 95% of the total flux. The magnification factor is

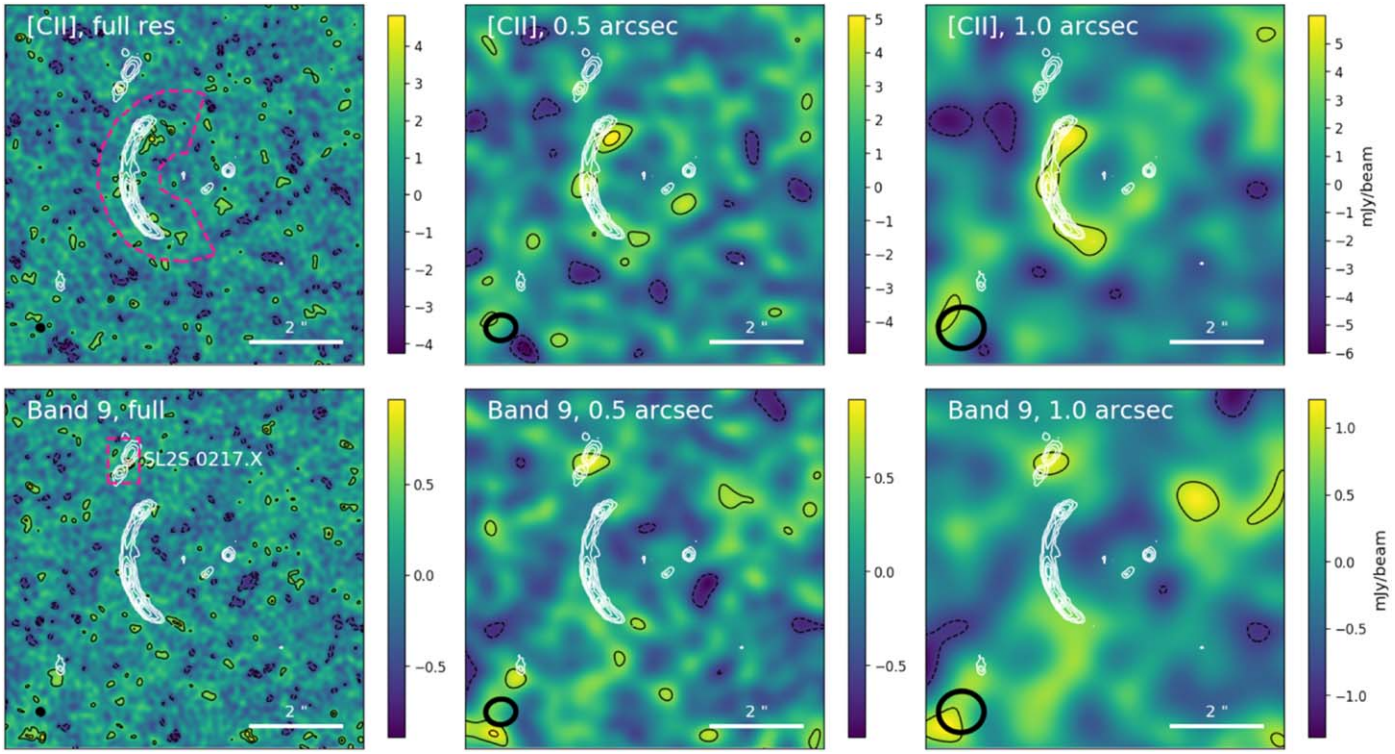

Figure 1. ALMA Band 9 imaging: dirty naturally weighted images of the [C II] line (upper) and continuum (lower) at full resolution and $0\farcs5$ and $1\farcs0$ taper, overlaid with the HST F606W imaging (Brammer et al. 2012; white contours). The [C II] emission is integrated over the 250 MHz (110 km s^{-1}) bandwidth centered at 667.97 GHz; this part of the spectrum shows the tentative 2σ–3σ extended emission. The black contours start at $\pm2\sigma$ and increase in steps of 1σ. The HST contours are drawn at 5%, 10%, 20%, 40%, 60%, and 80% of the surface brightness maximum. The dashed line (left) indicates the $R = 3$ kpc aperture used to extract the upper limits (see Section 3.1). No continuum emission from the main source is detected; the second lensed source (SL2S 0217.X, $z = 2.29$) is tentatively detected at 2σ–4σ significance in each image.

$\mu = 43$, 25, and 16 for the $R = 1$, 2, and 3 kpc apertures, respectively.

We note that in the synthesis imaging, the area under a dirty beam integrates to zero for large aperture sizes, unlike for a classical point-spread function. Consequently, flux measurements extracted from dirty images over extended areas might be biased, particularly in the presence of strong positive or negative side lobes. However, the dirty beams corresponding to the Figure 1 images are well described by a central Gaussian with only very small side lobes ($\leqslant$5%) within the apertures considered here. Our flux limits should therefore be robust.

Figure 2 shows the spectra extracted from within these apertures, at 100 MHz resolution, which reveal an excess flux at 667.9 GHz. The excess signal is unlikely to be caused by, e.g., continuum contamination or phase errors. At 250 MHz binning (110 km s^{-1}), the excess is detected at 3.2σ–4.3σ significance, depending on the taper and aperture used.

No continuum signal is detected at $\geqslant 3\sigma$ significance; we therefore put a conservative 3σ upper limit on the rest-frame 160 μm flux $S_{160\mu m} \leqslant 0.23$ mJy, based on the $1\farcs0$ taper images and the $R \leqslant 3$ kpc aperture.

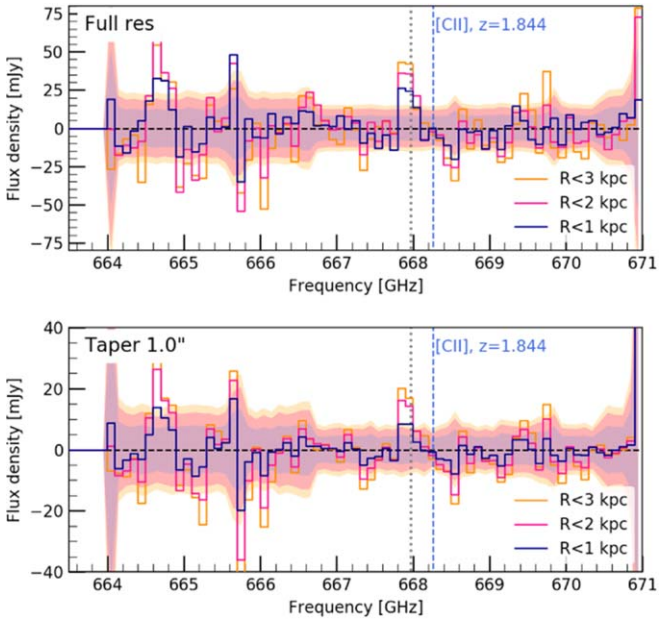

Figure 2. ALMA Band 9 spectrum of SL2S 0217 at 100 MHz (45 km s^{-1}) resolution, extracted for the full-resolution and $1\farcs0$ taper images, and the three source-plane apertures. The shaded regions indicate $\sigma_{\rm rms}$ for each channel. We obtain a tentative (3σ–4σ) [C II] 158 μm detection at 667.97 GHz (offset from the systemic velocity by $\sim$50 km s^{-1}).

3.1.2. Searching for the Signal in the (u, v) Plane

As the spatial filtering by the incomplete (u, v)-plane coverage might decrease the sensitivity to extended emission in the synthesized images, we try to confirm our tentative detection of the [C II] line in the (u, v) plane. How bright can the [C II] emission be to still be consistent with the observed visibilities?

We use the following approach by adapting the (u, v)-plane lens-modeling technique from Rybak et al. (2015) and Rybak (2017). First, we extract the visibility data (real and imaginary

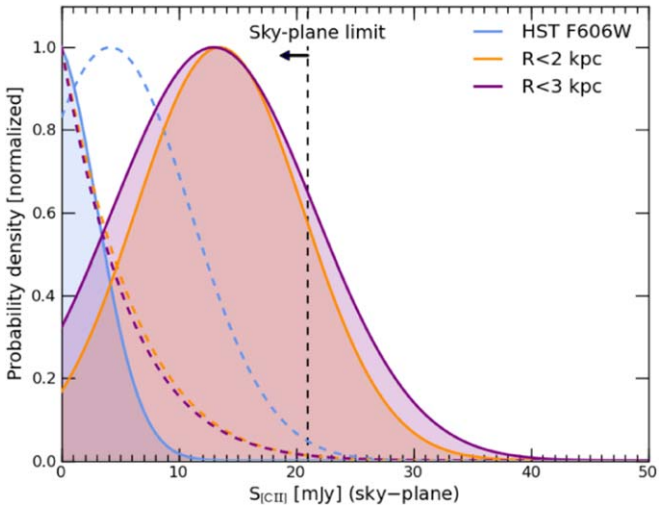

Figure 3. (u, v)-plane analysis of the ALMA [C II] 158 μm observations: probability distribution function (PDF) of the sky-plane [C II] flux for a 250 MHz bandwidth (see Figure 1), assuming different surface brightness distributions and compared to the sky-plane limit (21 mJy). Colored dashed lines indicate sky-flux PDFs for a "line-free" part of the data (i.e., where no signal is expected). Although the [C II] PDF peaks around 15 mJy for $R \leqslant 2$, 3 kpc apertures, this solution is not strongly preferred over the null hypothesis ($S_{[\mathrm{C\,II}]} = 0$ mJy) and is below the sky-plane limit. This result does not depend on the noise model used. We therefore adopt an upper limit on $S_{[\mathrm{C\,II}]} = 21$ mJy based on image-plane analysis.

parts) at 669.970 ± 0.125 GHz (the same bandwidth as used for the image-plane analysis). The noise on the real/imaginary visibilities is estimated by taking the rms of the visibilities for a given baseline for each individual scan. As the noise per polarization might differ, we do not combine the *XX* and *YY* polarizations into the Stokes *I*. We then calculate the expected signal $V(u, v)^{\mathrm{model}}$ for each visibility as

$$V(u, v)^{\mathrm{model}} = \sum_{l,m} B(l, m) I(l, m) e^{2\pi i(ul+vm)}, \quad (1)$$

where B is the primary beam response (approximated by a Gaussian), I the input sky brightness distribution, and m, l the sky-plane coordinates. We consider the following sky-plane [C II] surface brightness distributions: HST F606W arc (see Figure 1) and the $R \leqslant 1$, 2, and 3 kpc apertures; the total flux varies between 0 and 50 mJy. We calculate the log-likelihood value $\log L \propto -\sum_i (V(u_i, v_i)^{\mathrm{model}} - V(u_i, v_i)^{\mathrm{data}})^2/\sigma(u_i, v_i)^2$. As a control test, we perform the same analysis for a "line-free" part of the spectrum (680.000 ± 0.125 GHz).

Figure 3 shows the derived probability distribution function (PDF) for $S_{[\mathrm{C\,II}]}$. For the $R \leqslant 2$ kpc and $R \leqslant 3$ kpc apertures, the PDF peaks around $S_{[\mathrm{C\,II}]} = 15$ mJy, whereas for the HST-based aperture, the PDF peaks at 0 mJy. Reassuringly, the PDF for the "line-free" part of the spectrum peaks near $S_{[\mathrm{C\,II}]} = 0$ mJy (dashed lines) for all apertures. Tweaking the noise calculation (e.g., by combining the polarizations, calculating the rms over several scans) does not substantially change the PDFs. This might be indicative of an extended [C II] emission in SL2S 0217. However, the $S_{[\mathrm{C\,II}]} = 15$ mJy solution is not strongly preferred over the $S_{[\mathrm{C\,II}]} = 0$ mJy, our null hypothesis.

Consequently, we adopt a [C II] upper limit of $S_{[\mathrm{C\,II}]} \leqslant 21$ mJy over the 250 MHz (110 km s^{-1}) bandwidth, measured for the 1.″0 *uv* taper and $R \leqslant 3$ kpc source-plane aperture (3.2σ significance). The 1.″0 taper maximizes the surface brightness sensitivity, while the large aperture size accounts for a

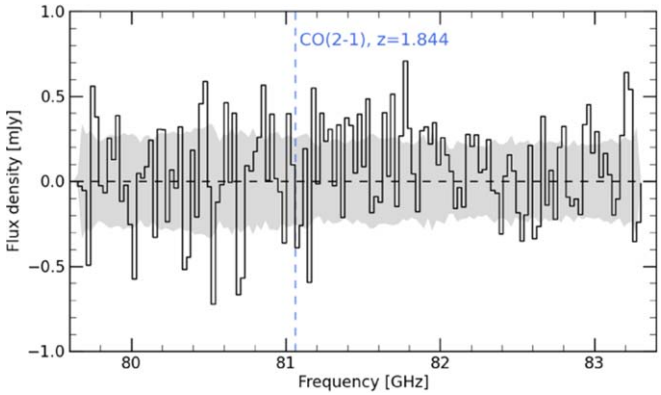

Figure 4. PdBI spectrum of SL2S 0217 with 100 km s^{-1} frequency bins. The shaded region indicates the σ_{rms} for each channel. We do not detect any significant CO(2–1) emission from SL2S 0217.

potentially very extended [C II] emission. This line flux corresponds to a sky-plane luminosity of $L_{[\mathrm{C\,II}]} \leqslant 3.4 \times 10^8\ L_\odot$; after delensing ($\mu = 16$), we set a source-plane upper limit of $L_{[\mathrm{C\,II}]} \leqslant 2.1 \times 10^7\ L_\odot$. The line width adopted here is comparable to the typical line FWHM of $\sim$120 km^{-1} of $z \sim 2$ EELGs (Maseda et al. 2014).

3.2. CO(2–1) Line

As shown in Figure 4, we do not detect any significant CO(2–1) line emission toward SL2S 0217; the PdBI spectrum is consistent with pure noise. Assuming the same aperture and 110 km s^{-1} line width as for the [C II] line (see Figure 1), we set a 3σ upper limit on $L_{\mathrm{CO(2-1)}} \leqslant 1.3 \times 10^5 L_\odot$, $L'_{\mathrm{CO(2-1)}} \leqslant 4 \times 10^8$ K km s^{-1} pc^2 (source plane).

4. Discussion

4.1. Photoionization Modeling

With an ionization energy of 11.3 eV, the [C II] 158 μm emission[17] can arise from all ISM phases: molecular (H_2), neutral (H), and ionized (H^+). Although studies of nearby galaxies have shown that at $Z \leqslant 0.25\,Z_\odot$ almost all [C II] emission arises from the neutral ISM (Croxall et al. 2017; Sutter et al. 2019); the large ionizing flux and limited self-shielding due to low metallicity in SL2S 0217 might cause the ionized component to dominate its $L_{[\mathrm{C\,II}]}$ (Ferrara et al. 2019). In SL2S 0217, the semiforbidden C II]2325 Å emission line and the C II absorption line detected in the Keck spectra (B18) confirm the presence of at least some C^+ in the ionized ISM. But *can* the ionized gas account for the entire [C II] 158 μm emission?

We address this question by using photoionization modeling to predict the [C II] 158 μm emission from the ionized ISM using the MAPPINGS V photoionization code (Allen et al. 2008; Groves & Allen 2010). We focus on the [C II] 158μm far-IR line and the rest-frame UV C II] 2325 Å line and the C III] 1909 Å doublet,[18] which are all predicted by MAPPINGS V. The photoionization modeling provides a lower limit on $L_{[\mathrm{C\,II}]}$, as the contribution of [C II] 158 μm from photon-dominated

[17] In this section, we explicitly state the wavelengths of individual emission lines for clarity.

[18] Here, we treat the ISM as uniform. However, as shown by E19, the UV spectral slope varies considerably across the source; the C II], [C II] and C III] lines are thus likely not cospatial on sub-kiloparsec scales.

regions (PDRs; e.g., Hollenbach & Tielens 1997) is not included in the MAPPINGS models. Due to the lack of constraints on the PDR phase (just our [C II] 158 μm and a very weak CO(2–1) upper limits), we refrain from modeling the neutral/molecular ISM.

The semiforbidden C III] 1909 Å doublet originates in the H II regions (e.g., Jaskot & Ravindranath 2016; Kewley et al. 2019; Vallini et al. 2020) and—thanks to its brightness—is a convenient tracer of ionized gas in the EoR (Stark et al. 2015, 2017; Zitrin et al. 2015); the C II] 2325 Å line traces the outer layers of H II regions, which also emit the [C II] 158 μm line. Based on our upper limits and B18 spectroscopy, the observed ratios are [C II] 158 μm/C II] 2325 Å $\leqslant$ 4.7, [C II] 158 μm/C III] 1909 Å $\leqslant$ 0.8, and C III] 1909 Å/C II] 2325 Å $= 6.2 \pm 0.5$ (in W m^{-2} units). Using C II] instead of any of the other UV lines detected in the Keck spectrum by B18 avoids systematic uncertainties related to the carbon abundance and ionization state.

To set the ionizing radiation field, we use the STARBURST99 stellar population models[19] (Leitherer et al. 1999, 2010), including also the effects of stellar rotation on the emitted spectra of massive stars, as described in Levesque et al. (2012).

Following the B18 modeling of the UV spectrum, we set the model metallicity to 0.05 $Z_\odot$ and assume an instantaneous starburst. We explore models with electron densities between $n_e = 10$ and 100 cm^{-3}, as the C II] 2325 Å/ [C II] 158 μm flux ratio is very sensitive to density due to the low critical density of the [C II] 158 μm line in ionized gas ($n_e = 50$ cm^3). We vary the ionization parameter U (defined as the ratio of the $\geqslant$13.6 eV photon number density and the gas density n) and the age of the ionizing star cluster (in steps of 0.5 Myr). We adopt a one-dimensional plane-parallel geometry as appropriate for the expected geometry in SL2S 0217: a screen of ionized ISM in front of an ionizing cluster. Figure 5 shows the predicted [C II] 158 μm/C II] 2325 Å and C III] 1909 Å/C II] 2325 Å ratios for each realization.

The C III] 1909 Å/C II] 2325 Å ratio depends on both the ionization parameter (impacting both the gas temperature and ionization state) and the age of the starburst (affecting the relative number of C^+ ionizing photons, >24.4 eV, to C^0 ionizing photons, >11.3 eV). See Jaskot & Ravindranath (2016) and Kewley et al. (2019) for other examples, and the color axes in Figure 5.

As the [C II] 158 μm and C II] 2325 Å lines arise only from a single species and ionization state, their ratio is purely dependent upon the electron density and temperature, which drive the relative collisional rates. Because of the low critical density for [C II] 158 μm ($n_e \simeq 50$ cm^{-3}) and high excitation energy of the C II] 2325 Å line, the [C II] 158 μm/C II] 2325 Å ratio depends strongly on both electron density and temperature.

We find that, for $n_e = 100$ cm^{-3} (the value assumed by B18), MAPPINGS predicts $\log(L^{\rm ion}_{[\rm C\,II]158\,\mu m}/L_{[\rm C\,II]2325\,Å}) \sim -0.5 \pm 0.5$ (Figure 5). For $n_e = 10$ cm^{-3}, the ratio is typically 0.5 dex higher, as the critical density for [C II] 158 μm is lower than for C II]2325 Å. Therefore, we conservatively assume that $\log(L^{\rm ion}_{[\rm C\,II]158\,\mu m}/L_{[\rm C\,II]2325\,Å}) = 0 \pm 1$. Given the [C II]2325 Å flux of 1.11×10^{-17} erg s^{-1} cm^{-2} (flux of the brightest line in the C II] triplet, measured by B18; this is the line predicted by MAPPINGS), we estimate an on-sky [C II] 158 μm line luminosity $L^{\rm ion}_{[\rm C\,II]158\,\mu m} \sim 7.3 \times 10^7\,L_\odot$.

This estimate is approximately 5× lower than our [C II] 158 μm upper limit ($L^{\rm sky}_{[\rm C\,II]158\,\mu m} \leqslant 3.4 \times 10^8\,L_\odot$) although the lack of n_e constraints implies a ~1 dex uncertainty in the predicted flux ratio.

For most of the n_e, U models considered here, our [C II] 158 μm upper limit is higher than the contribution from the ionized ISM; the neutral/molecular ISM can account for up to 80% of the [C II] 150 μm line flux, similar to the $z = 0$ low-metallicity galaxies (Croxall et al. 2017; Cormier et al. 2019). However, in the low-density, high-ionization regime ($n_e = 10$ cm^{-3}, log $U \geqslant -3.5$), the predicted [C II] 158 μm luminosity exceeds our upper limits. In such case, the ISM in SL2S 0217 will be fully ionized.

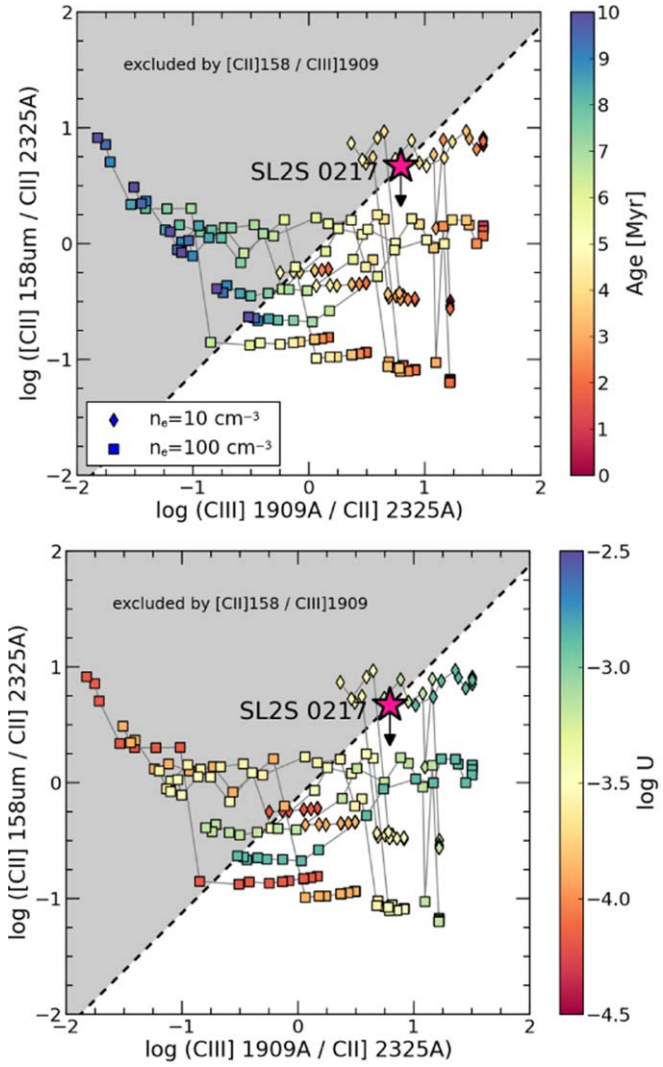

Figure 5. MAPPINGS modeling of C^+/C^{2+} emission lines from the ionized ISM as a function of the starburst age (upper) and the ionization parameter U (lower). We show the ratios of the [C II] 158 μm, C II] 2325 Å. and C III] 1909 Å luminosities for an instantaneous star formation burst, $Z = 0.05\,Z_\odot$, $n_e = 10$, and 100 cm^{-3}. The gray lines connect models with constant U and increasing age. The shaded area is excluded by the [C II] 158 μm/C III] 1909 Å ratio. The upper limit on $L_{[\rm C\,II]}$ is consistent with a young (<5 Myr) starburst over a wide range of U and allows for a substantial [C II] emission from the neutral ISM.

[19] For the case considered here, the predicted line intensities differ only marginally ($\leqslant$0.1 dex) between the different stellar model libraries. See D'Agostino et al. (2019) for a detailed comparison.

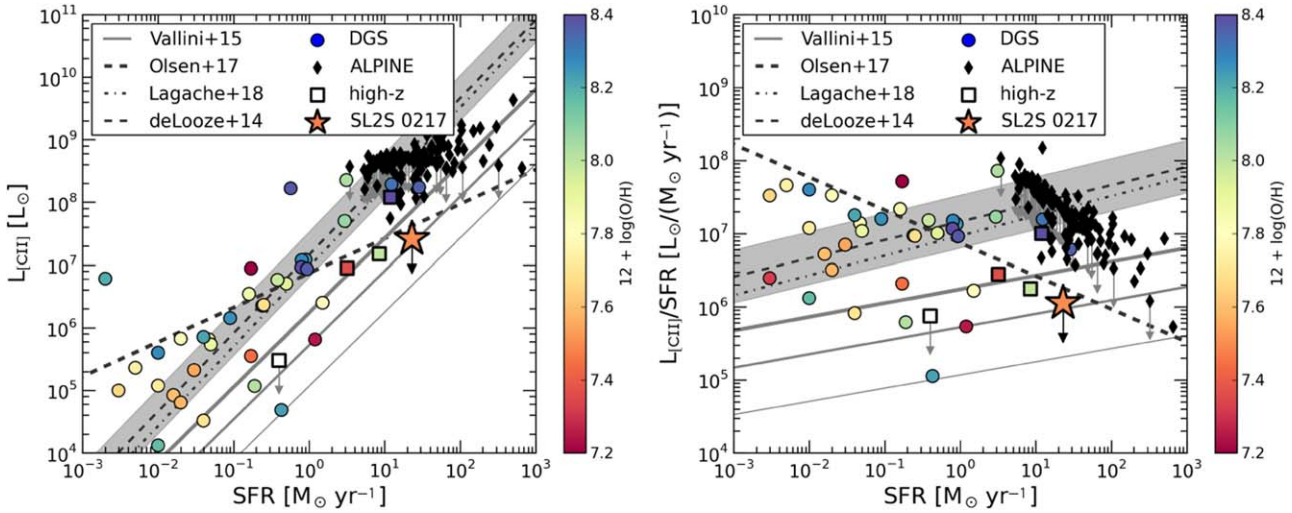

Figure 6. [C II] luminosity (left) and the [C II]/SFR ratio vs. SFR (right) in SL2S 0217, compared to the nearby Dwarf Galaxy Survey (Cormier et al. 2015, 2019) and ALPINE samples (Schaerer et al. 2020), and $z = 2$–7 observations of low-mass galaxies (Schaerer et al. 2015; Knudsen et al. 2016; Bradač et al. 2017), colored by 12 + log (O/H). For the ALPINE sources, we use the publicly available SED-based SFR estimates from Faisst et al. (2020). The different lines indicate different models from Table 3: Vallini et al. (2015) for $Z = 0.025$ (thinnest line), 0.05, and 0.1 $Z_\odot$ (thickest); De Looze et al. (2014; with 1σ scatter indicated by shading); Olsen et al. (2017); and Lagache et al. (2018). We do not show the Herrera-Camus et al. (2015) relation, as it generally predicts a higher $L_{[C\,II]}$ than De Looze et al. (2014) over the SFR range studied here. The [C II]/SFR ratio in SL2S 0217 is at least 30× lower than predicted by the De Looze et al. (2014) relation.

Table 3
[C II]–SFR Relations Referenced in This Work, with the Expected [C II]/SFR Ratio for SL2S 2017, Given the Parameters from Table 1

Reference	[C II]–SFR	$L_{[C\,II]}/SFR$ $[L_\odot/(M_\odot\,yr^{-1})]$	Note
De Looze et al. (2014)	$\log L_{[C\,II]} = 1.25\log(SFR) + 7.16$	3×10^7	Local dwarf galaxies (Cormier et al. 2015)
Herrera-Camus et al. (2015)	$\log L_{[C\,II]} = 0.97\log(SFR) + 7.66$	4×10^7	Local star-forming galaxies
Vallini et al. (2015)	$\log L_{[C\,II]} = 7.0 + 1.2\log(SFR) + 0.021\log(Z)+$ $+0.012\log(SFR)\log(Z) - 0.74\log^2(Z)$	9×10^5	Zoom-in simulations, $z = 6.6$ $Z = 0.05 - 1\ Z_\odot$, SFR=1-100 $M_\odot$ yr^{-1}
Olsen et al. (2017) [a]	$\log L_{[C\,II]} = 7.17 + 0.55\log SFR + 0.23\log Z$	1.8×10^6	Zoom-in simulations, $z \sim 6$, $M_\star = (6\text{–}80) \times 10^8\ M_\odot$, SFR = 3–20 $M_\odot$ yr^{-1}, $Z = 0.16$–$0.45\ Z_\odot$
Lagache et al. (2018) [b]	$\log L_{[C\,II]} = 7.1 + (1.4 - 0.07z)\log(SFR)$- $-0.07z$	2.2×10^7	Semianalytic models, $z = 4$–7 $Z = 0.004$–$4.4\ Z_\odot$

Notes. The [C II]/SFR ratio in SL2S 0217 is $\leqslant 1 \times 10^6\ L_\odot/(M_\odot\ yr^{-1})$.
[a] Not correcting for the CMB temperature effects, which are negligible at $z \sim 2$ (see Olsen et al. 2018 erratum).
[b] No metallicity dependence, weak evolution with redshift z.

4.2. Comparison with Empirical Models and Simulations

We now compare SL2S 0217 to predictions for [C II] luminosity from various empirical models and hydrodynamical simulations. Thanks to the stream of high-redshift [C II] detections from ALMA (Hodge & da Cunha 2020), the [C II] emission from high-redshift galaxies has been extensively studied by a number of high-resolution hydrodynamical simulations. Our tentative [C II] detection in a $Z = 0.05\ Z_\odot$ dwarf allows us to validate these models in the poorly explored high-SFR, low-metallicity regime.

Namely, we consider the following [C II]–SFR relations: the empirical De Looze et al. (2014) relation for nearby low-metallicity dwarf galaxies, the Herrera-Camus et al. (2015) calibration for nearby star-forming galaxies, as well as predictions from simulations of Vallini et al. (2015), Olsen et al. (2017), and Lagache et al. (2018). Table 3 lists the respective [C II]–SFR relations and the predicted source-plane [C II]/SFR ratio for SL2S 0217. Figures 6 and 7 compare the $L_{[C\,II]}$ and $L_{[C\,II]}/SFR$ in SL2S 0217 with relations from Table 3, and low- and high-redshift observations (see below) as a function of SFR and metallicity.

Our upper limit is in agreement with the metallicity-dependent relations of Vallini et al. (2015) and Olsen et al. (2017). On the other hand, the [C II] emission in SL2S 0217 is at least 30× fainter than expected from the locally calibrated De Looze et al. (2014) relation, a $\geqslant 4\sigma$ tension. The Herrera-Camus et al. (2015) relation predicts an even higher $L_{[C\,II]}/SFR$ with a smaller scatter (∼0.2 dex); this is likely a consequence of the relatively high metallicity of their sample (12 + log(O/H) = 7.7–8.8).

Finally, Lagache et al. (2018) underpredict the SL2S 0217 [C II] luminosity by a factor of 20; however, given the 0.5 dex 1σ scatter of the Lagache et al. (2018) trend, our upper limit is still consistent with it at the 2.5σ level. We note that the Lagache et al. (2018) simulations contain a significant number of galaxies with SFR, metallicity, and $L_{[C\,II]}$ consistent with SL2S 0217.

The strong dependence of the $L_{[C\,II]}/SFR$ ratio on the average gas metallicity is supported by the high-resolution

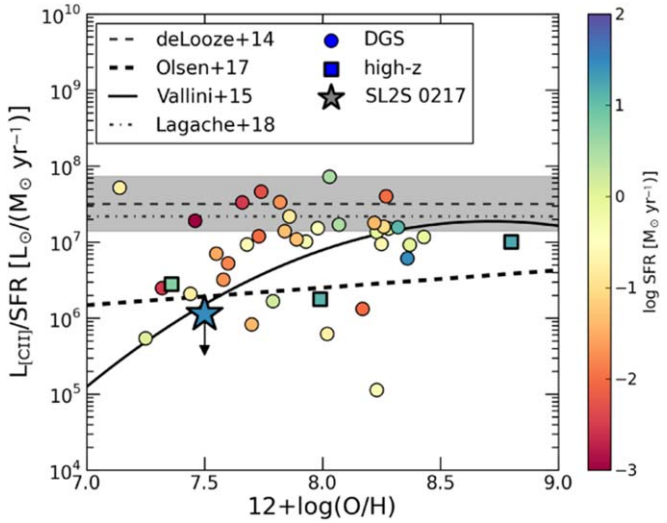

Figure 7. [C II]/SFR ratio as a function of metallicity: comparison of SL2S 0217 to the Cormier et al. (2015), Knudsen et al. (2016), and Bradač et al. (2017) sources (color-coded by SFR), and the different relations from Section 4.2, all for SL2S 0217–like SFR $= 23\ M_\odot\ yr^{-1}$. The [C II]/SFR ratio in SL2S 0217 is consistent with the metallicity-dependent relations of Vallini et al. (2015) and Olsen et al. (2017), but much lower than predicted by De Looze et al. (2014) and Lagache et al. (2018).

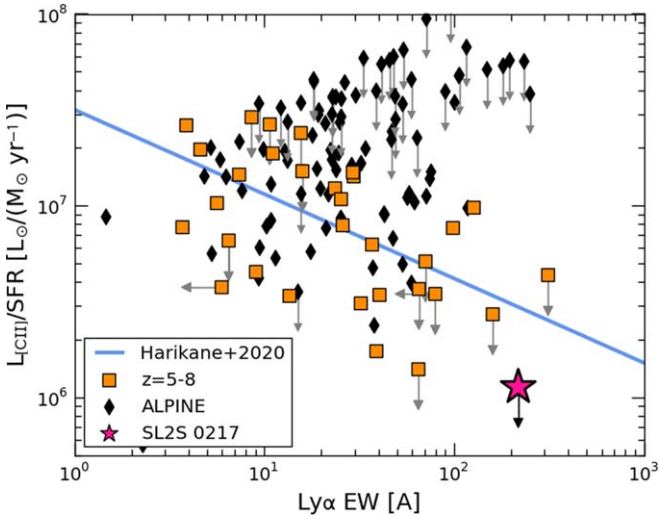

Figure 8. Upper limits on the [C II]/SFR ratio in SL2S 0217 vs. the Lyα equivalent width (E19), compared to the Harikane et al. (2018) and Matthee et al. (2019) compilations of $z = 5$–7 Lyα emitters and the $z = 4.4$–5.9 ALPINE survey (Schaerer et al. 2020). SL2S 0217 is a factor of 3 below the empirical relation of Harikane et al. (2020).

simulations of high-z dwarf galaxies by Lupi & Bovino (2020): for $Z \leqslant 0.1\ Z_\odot$, they find $L_{[C\ II]}/SFR \leqslant 10^6\ L_\odot/(M_\odot\ yr^{-1})$, consistent with our upper limit.

Finally, we consider the analytical model of Ferrara et al. (2019), who investigated the low [C II] luminosities of some of the high-z, UV-selected sources. In the low-metallicity, high-Σ_{SFR} regime of SL2S 0217, the [C II] surface density $\Sigma_{[C\ II]}$ (in units of $L_\odot$ kpc^{-2}) is given by

$$\Sigma_{[C\ II]} = 1.8 \times 10^7 \left(\frac{n_{gas}}{n_{500}}\right) \ln\left(\frac{U}{0.001}\right), \quad (2)$$

where $n_{500} = 500\ cm^{-3}$. For SL2S 0217, with an ionization parameter log $U = -1.5$ (B18) and assuming that [C II] is cospatial with the UV continuum, Equation (2) matches our $\Sigma_{[C\ II]}$ upper limit for $n_{gas} \simeq 150\ cm^{-3}$ (n_{gas} decreases further if [C II is more extended than the UV continuum). As the Ferrara et al. model directly sets $U \propto \Sigma_{SFR}/\Sigma_{gas}^2$, to reconcile the high U and $\langle\Sigma_{SFR}\rangle$, SL2S 0217 has to be an extreme starburst, with a gas surface density $\Sigma_{gas} \simeq 3.5 \times 10^8\ M_\odot\ kpc^{-2}$. This roughly agrees with the expectation from the E19 gas column-density estimate $N_{H\ I} \simeq 10^{21.7}\ cm^{-3}$, which predicts $\Sigma_{gas} = N_{H\ I} \times m_{proton} \simeq 8 \times 10^7\ M_\odot\ kpc^{-2}$.

4.3. Comparison with Low-metallicity Galaxies Near and Far

In the present-day universe, SL2S 0217 can be directly compared to galaxies from the Dwarf Galaxy Survey (DGS) (Madden et al. 2013), which span $Z = 0.02$–$1.0\ Z_\odot$ and SFR $= 0.0005$–$25\ M_\odot\ yr^{-1}$; 48 galaxies from the DGS sample were targeted with Herschel PACS far-IR spectroscopy by Cormier et al. (2015). Although the DGS sample shows a broad [C II]/SFR correlation, the [C II]/SFR ratio varies between $10^{5.0}$ and $10^{9.5}\ L_\odot/(M_\odot\ yr^{-1})$ (Figure 6). Four DGS sources have [C II]/SFR ratios similar to or lower than SL2S 0217. In particular, SBS 0335–052—which matches SL2S 0217 in terms of the rest-frame UV line ratios and the overall SED (E18)—has [C II]/SFR $\simeq 5.5 \times 10^5\ L_\odot/(M_\odot\ yr^{-1})$, directly comparable to our upper limits.

At $z = 1$–2, the bulk of [C II] and CO molecular gas studies have focused on relatively massive galaxies with $M_\star \geqslant 10^{10}\ M_\odot$ (e.g., Stacey et al. 2010; Brisbin et al. 2015; Zanella et al. 2018). The only exception is the strongly lensed $M_\star \simeq 2.5 \times 10^9 M_\odot$ galaxy detected in [C II] and CO(3–2) by Schaerer et al. (2015); however, it is still $\sim 10\times$ more massive and metal enriched than SL2S 0217. The [C II]/SFR ratio measured by Schaerer et al. (2015) is $10^7\ L_\odot/(M_\odot\ yr^{-1})$, 1 dex higher than in SL2S 0217.

At $z \geqslant 6$, two $z = 6$–7 EELGs lensed by galaxy clusters have been detected in the [C II] emission by Knudsen et al. (2016, who also obtained a strong upper limit on another source) and Bradač et al. (2017). Similar to SL2S 0217, all three sources have [C II]/SFR $\leqslant 3 \times 10^6$, significantly lower than the locally calibrated De Looze et al. (2014) relation (Figure 6). While the Knudsen et al. (2016) [C II]-detected source has a relatively low SFR and high stellar mass ($M_\star \simeq 3 \times 10^9\ M_\odot$), the Bradač et al. (2017) source is very similar to SL2S 0217, with SFR $\simeq 9\ M_\odot\ yr^{-1}$, $M_\star \simeq 10^8\ M_\odot$, and $Z = 0.2\ Z_\odot$.

At higher stellar masses ($M_\star = 10^9$–$10^{11}\ M_\odot$), the ALPINE ALMA large program (Faisst et al. 2020; Bethermin et al. 2020; Le Fèvre et al. 2020) has recently observed the [C II] line in 189 $z = 4$–6 galaxies with SFR $= 1$–$100\ M_\odot\ yr^{-1}$ (Schaerer et al. 2020). The ALPINE sources are generally consistent with the De Looze et al. (2014) relation and have higher [C II]/SFR than SL2S 0217, likely due to their presumably higher metallicity (23 out of 118 ALPINE sources are detected in the rest-frame 160 μm continuum indicating substantial dust masses; Bethermin et al. 2020).

Finally, Figure 8 compares the [C II] luminosity and [C II]/SFR ratio in SL2S 0217 to the compilation of $z = 5$–7 Lyα emitters (Harikane et al. 2018; Matthee et al. 2019) and the ALPINE survey (Schaerer et al. 2020). The Lyα EW correlates closely with the Lyα photon escape fraction (e.g., Verhamme et al. 2017; Harikane et al. 2018; Matthee et al. 2019); the sources with high Lyα EW are thus expected to be depleted in neutral ISM. For SL2S 0217, E19 derived a photometric

EW $= 218 \pm 12$ Å. Compared to the $z \geqslant 5$ Lyα emitters, SL2S 0217 has a low [C II]/SFR ratio and is a factor of $\sim$3 below the Harikane et al. (2020) empirical Lyα EW–[C II]/SFR relation. The low [C II]/SFR ratio in SL2S 0217 might be driven by its relatively compact size: its source-plane $R_{1/2}^{\rm UV} \sim 0.35$ kpc, compared to $\sim$1 kpc radii for $z \sim 6$ sources (Carniani et al. 2018, 2020; Matthee et al. 2019), which might increase the ionized ISM fraction, suppressing the [C II] emission.

4.4. The Fate of Molecular Gas in SL2S 0217

Given the upper limits on the [C II] and CO(2–1) luminosity, what can we say about the state of the molecular gas in SL2S 0217? Does SL2S 0217 still contain a substantial molecular gas reservoir, or is it at the very end of its starburst phase, with the ISM depleted and ionized? We briefly discuss three facets of this problem: (i) limits on the molecular gas mass, (ii) the possibility of the ISM being fully ionized, and (iii) photoevaporation of molecular gas.

First, adopting the conservative magnification factor $\mu = 16$, the CO(2–1) upper limit translates to a (very weak) 3σ upper limit $M_{\rm H_2} \leqslant 2 \times 10^9\, M_\odot$, where we assume $r_{2/1} = 0.6$ (Cormier et al. 2014) and a Galactic $\alpha_{\rm CO} = 4.4 M_\odot/({\rm K\,km\,s^{-1}\,pc^2})$. However, studies of nearby low-metallicity dwarfs (e.g., Schruba et al. 2012; Hunt et al. 2015; Shi et al. 2016) found $\alpha_{\rm CO}$ up to 3 dex higher than the Galactic value, significantly weakening our $M_{\rm gas}$ upper limit.

Alternatively, we can estimate the molecular gas mass $M_{\rm H_2}$ from the [C II] luminosity, as originally proposed by Zanella et al. (2018). Due to the very low metallicity of SL2S 0217, rather than using the Zanella et al. (2018) relation (see below), we use the recently published relation of Madden et al. (2020) calibrated on the DGS sample:

$$M_{\rm H_2}^{\rm [C\,II]}\,({\rm M20}) = 132 \times L_{\rm [C\,II]}^{0.97}, \quad (3)$$

which for SL2S 0217 yields $M_{\rm H_2} \leqslant 2.1 \times 10^9\, M_\odot$. Alternatively, using the Zanella et al. (2018) relation calibrated on more massive main-sequence galaxies:

$$M_{\rm H_2}^{\rm [C\,II]}\,({\rm Z18}) = 31 \times L_{\rm [CII]}, \quad (4)$$

we obtain $M_{\rm H_2} \leqslant 0.8 \times 10^9\, M_\odot$, although the extrapolation of the Zanella et al. (2018) relation to the low-Z regime might not be straightforward. Both $M_{\rm gas}$ estimates imply a high gas mass fraction $f_{\rm gas} = M_{\rm gas}/(M_{\rm gas} + M_\star) \simeq 0.8$. This is consistent with high gas fractions and dynamical mass estimates for $z = 1$–2 EELGs (Maseda et al. 2014) and simulations of high-redshift dwarf galaxies (Ceverino et al. 2018).

A gas mass of $\sim 10^8\, M_\odot$ is also supported by the expectations from the Ferrara et al. (2019) model and the column-density estimates from E19 (see Section 4.2).

A gas mass of $10^8\, M_\odot$ is further supported by the high $\Sigma_{\rm SFR}/U$ ratio in SL2S 0217 (see Section 4.2). With SFR $= 23\, M_\odot\,{\rm yr}^{-1}$, SL2S 0217 will deplete its gas in $\sim$10 Myr (likely much faster, as some gas might be expelled from the system). This suggests that SL2S 0217 is in a final stage of an intense starburst.

Second, as indicated in Section 4.1, a substantial fraction of the gas reservoir might be ionized. Namely, the maximum column density proposed by E19 ($\Sigma_{\rm H\,I} \leqslant 10^{21.7}$ cm^{-2}) is comparable to the ionized gas column depth of $\sim 10^{21.3}$ cm^{-2} predicted by Ferrara et al. (2019) for SL2S 0217–like ionization parameter and metallicity. The fraction of the ionized gas might be further increased due to additional ionizing sources. In particular, the unusually strong He II emission in SL2S 0217 cannot be reproduced by standard photoionization models (B18) and requires additional ionization source, such as radiative shocks (Allen et al. 2008; Plat et al. 2019) or high-mass X-ray binaries as seen in, e.g., a nearby dwarf I Zw 18 (Lebouteiller et al. 2017; Schaerer et al. 2019, but see Plat et al. 2019). This extra ionization would increase the contribution of the ionized ISM to the [C II] luminosity compared to our photoionization models; on the other hand, strong FUV fields might suppress the [C II] emission by ionizing C^+ into C^{2+} (e.g., Langer & Pineda 2015).

Third, the combination of the strong FUV fields and the lack of ISM self-shielding at low metallicities can lead to a rapid ionization and photoevaporation of the molecular clouds on 1–10 Myr timescales, thus further suppressing the [C II] emission (Vallini et al. 2017).

We note that in the very near future, the warm neutral or molecular gas might be traced at mid-infrared wavelengths via the PAHs or rotational-vibrational H_2 emission using the James Webb Space Telescope. Alternatively, the gas mass in SL2S 0217 can be constrained kinematically (e.g., Calistro Rivera et al. 2018), using the integrated-field spectroscopy of the bright C III] 1909 Å line (M. Maseda et al. 2021, in preparation).

4.5. Detectability of [C II] Emission from Metal-poor Dwarfs at z $\geqslant$ 6

What are the prospects of detecting the [C II] 158 μm emission in SL2S 0217 if it was at $z \sim 6$? Assuming $L_{\rm [C\,II]} = 2.6 \times 10^7\ L_\odot$, achieving a spatially unresolved 5σ detection at $z = 6$ would require $\sigma_{\rm rms} \sim 50\,\mu$Jy over the 100 km s^{-1} bandwidth, which corresponds to $\sim$10 hr of ALMA on-source time. For comparison, the deepest ALMA Band 6 observations to date, delivered by the ASPECS (Walter et al. 2016; González-López et al. 2020) and ALMACAL (Oteo et al. 2016) projects and the Fujimoto et al. (2016) compilation, reach sensitivities of $\sigma_{\rm rms} \sim 100\,\mu$Jy over the same bandwidth.

Another promising way of studying the population of galaxies at high redshift is the line-intensity mapping (e.g., Gong et al. 2012; Silva et al. 2015). The feasibility of the [C II]-intensity mapping measurements depends critically on the [C II] luminosity function at $z \geqslant 6$. A recent [C II]-intensity mapping feasibility study of Yue & Ferrara (2019) considered several [C II] luminosity function models. The detectability of the [C II] power spectrum is the highest for the De Looze et al. (2014) dwarf galaxy relations and the lowest for the Vallini et al. (2015) relation; the predictions for the expected power spectrum and shot-noise signal from the two models differ by a factor of $\sim$30. Consequently, if the low [C II]/SFR ratio in SL2S 0217 can be taken to validate the Vallini et al. (2015) and Olsen et al. (2017) [C II] luminosity models, the $z \geqslant 6$ [C II] intensity mapping signal will fall below the detection threshold of the potential ALMA or single-dish intensity mapping experiments (e.g., a 1000 hr program on the CCAT-p telescope, Stacey et al. 2018). Our analysis highlights the need to properly account for the metallicity evolution of galaxies and its impact on the [C II] emission.

5. Summary and Conclusions

We have presented deep ALMA and PdBI observations of the [C II] 158 μm and CO(2–1) emission in the $z = 1.844$ strongly lensed metal-poor dwarf galaxy SL2S 0217. In one of the deepest ALMA Band 9 observations to date, we obtain a tentative 3σ–4σ detection of the [C II] line. No CO(2–1) emission is detected in the PdBI observations. Our main conclusions are as follows:

1. We report a tentative (3σ–4σ) detection of the [C II] line based on the image-plane spectra; the source-plane luminosity is $L_{[\mathrm{C\,II}]} \leqslant 2.6 \times 10^7\ L_\odot$, derived from 1.″0 taper imaging, $R \leqslant 3$ kpc aperture, and a 250 MHz bandwidth. We do not find strong evidence for [C II] emission in the (u, v) plane. The rest-frame 160 μm continuum and the CO(2–1) line are not detected. Our tentative [C II] detection extends the molecular gas studies at $z \sim 2$ by 1 dex in stellar mass, down to the $M_\star \simeq 10^8\ M_\odot$ regime.
2. The upper limit on the $L_{[\mathrm{C\,II}]}$/SFR ratio in SL2S 0217 is $2 \times 10^6\ L_\odot/(M_\odot\ \mathrm{yr}^{-1})$, within the range spanned by nearby dwarf galaxies (Cormier et al. 2015), as well as $z \geqslant 5$ lensed dwarf EELGs and Lyα emitters.
3. The [C II]/ SFR ratio in SL2S 0217 is consistent with the Vallini et al. (2015) and Olsen et al. (2017) simulation-based models. However, the [C II]/SFR ratio in SL2S 0217 is 30× lower than predicted by the locally calibrated De Looze et al. (2014) relation.
4. We use MAPPINGS photoionization modeling to predict the fraction of [C II] emission arising in the ionized ISM. We find that our upper limit leaves room for a significant (up to 80%) contribution from the PDRs; however, we cannot exclude that the ISM is fully ionized, particularly for low electron density. The contribution from the ionized ISM might be boosted due to extra ionizing radiation from, e.g., shocks or X-ray binaries. Future ALMA and JWST observations of PDR tracers will allow us to directly probe the neutral/molecular ISM.
5. The tentative [C II] detection and the high Σ_{SFR} and ionization parameter suggest a gas mass of a few $10^8\ M_\odot$. In this scenario, SL2S 0217 will be in a late phase of an extreme starburst and deplete its gas reservoir in <10 Myr. More robust constraints on the gas mass might be obtained from spatially resolved spectroscopic observations of the bright rest-frame FUV lines.
6. If SL2S 0217 is representative of the $z \geqslant 6$ low-mass galaxies, these will be within reach of deep-field ALMA observations (even without gravitational lensing). On the other hand, a strong dependence of the [C II]/SFR ratio on metallicity might strongly suppress the [C II] signal in line-intensity mapping experiments.

The large discrepancy between the [C II]/SFR ratio in SL2S 0217 and the widely used De Looze et al. (2014) relation for present-day dwarf galaxies highlights the limitations of applying locally established relations to high redshift. At the same time, the good agreement between our tentative [C II] detection, high-redshift observations, and simulations confirms that—though challenging to study—SL2S 0217 remains a powerful analog of the sources from the EoR.

We thank the anonymous referee for the careful and constructive review of this manuscript which improved the content and clarity of this paper.

This paper makes use of the following ALMA data: ADS/JAO.ALMA #2016.1.00142.S and #2016.1.00776.S. ALMA is a partnership of ESO (representing its member states), NSF (USA) and NINS (Japan), together with NRC (Canada), MOST and ASIAA (Taiwan), and KASI (Republic of Korea), in cooperation with the Republic of Chile. The Joint ALMA Observatory is operated by ESO, AUI/NRAO, and NAOJ. This work is based on observations carried out under project number X037 with the IRAM PdBI Interferometer. IRAM is supported by INSU/CNRS (France), MPG (Germany), and IGN (Spain).

M.R. and J.A.H. acknowledge support of the VIDI research program with project number 639.042.611, which is (partly) financed by the Netherlands Organisation for Scientific Research (NWO). M.R. acknowledges support from the Leids Kerkhoven-Bosscha Fonds, subsidy number 19.2.075. E.d.C. gratefully acknowledges the Australian Research Council as the recipient of a Future Fellowship (project FT150100079) and the ARC Centre of Excellence for All Sky Astrophysics in 3 Dimensions (ASTRO 3D; project CE170100013). M.A. has been supported by the grant "CONICYT + PCI + INSTITUTO MAX PLANCK DE ASTRONOMIA MPG190030" and "CONICYT+PCI+REDES 190194." D.K.E. is supported by the US National Science Foundation through the Faculty Early Career Development (CAREER) Program, grant AST-1255591. C.P. is supported by the Canadian Space Agency under a contract with NRC Herzberg Astronomy and Astrophysics.

Facilities: ALMA, IRAM:Interferometer.

ORCID iDs

Matus Rybak https://orcid.org/0000-0002-1383-0746
E. da Cunha https://orcid.org/0000-0001-9759-4797
B. Groves https://orcid.org/0000-0002-9768-0246
J. A. Hodge https://orcid.org/0000-0001-6586-8845
M. Aravena https://orcid.org/0000-0002-6290-3198
M. Maseda https://orcid.org/0000-0003-0695-4414
L. Boogaard https://orcid.org/0000-0002-3952-8588
D. Berg https://orcid.org/0000-0002-4153-053X
S. Charlot https://orcid.org/0000-0003-3458-2275
R. Decarli https://orcid.org/0000-0002-2662-8803
D. K. Erb https://orcid.org/0000-0001-9714-2758
E. Nelson https://orcid.org/0000-0002-7524-374X
C. Pacifici https://orcid.org/0000-0003-4196-0617
K. B. Schmidt https://orcid.org/0000-0002-3418-7251
F. Walter https://orcid.org/0000-0003-4793-7880
A. van der Wel https://orcid.org/0000-0002-5027-0135

References

Allen, M. G., Groves, B. A., Dopita, M. A., Sutherland, R. S., & Kewley, L. J. 2008, ApJS, 178, 20
Amorín, R., Pérez-Montero, E., Contini, T., et al. 2015, A&A, 578, A105
Asplund, M., Grevesse, N., Sauval, A. J., & Scott, P. 2009, ARA&A, 47, 481
Atek, H., Richard, J., Jauzac, M., et al. 2015, ApJ, 814, 69
Atek, H., Siana, B., Scarlata, C., et al. 2011, ApJ, 743, 121
Berg, D. A., Erb, D. K., Auger, M. W., Pettini, M., & Brammer, G. B. 2018, ApJ, 859, 164
Bethermin, M., Fudamoto, Y., Ginolfi, M., et al. 2020, A&A, 643, A2
Bouwens, R. J., Illingworth, G. D., Franx, M., et al. 2009, ApJ, 705, 936

Bradač, M., Garcia-Appadoo, D., Huang, K.-H., et al. 2017, ApJL, 836, L2
Brammer, G. B., Sánchez-Janssen, R., Labbé, I., et al. 2012, ApJL, 758, L17
Brisbin, D., Ferkinhoff, C., Nikola, T., et al. 2015, ApJ, 799, 13
Calistro Rivera, G., Hodge, J. A., Smail, I., et al. 2018, ApJ, 863, 56
Carniani, S., Ferrara, A., Maiolino, R., et al. 2020, MNRAS, 499, 5136
Carniani, S., Maiolino, R., Amorin, R., et al. 2018, MNRAS, 478, 1170
Carniani, S., Maiolino, R., Pallottini, A., et al. 2017, A&A, 605, A42
Ceverino, D., Klessen, R. S., & Glover, S. C. O. 2018, MNRAS, 480, 4842
Cooray, A., Fu, H., Calanog, J., et al. 2011, arXiv:1110.3784
Cormier, D., Abel, N. P., Hony, S., et al. 2019, A&A, 626, A23
Cormier, D., Madden, S. C., Lebouteiller, V., et al. 2014, A&A, 564, A121
Cormier, D., Madden, S. C., Lebouteiller, V., et al. 2015, A&A, 578, A53
Croxall, K. V., Smith, J. D., Pellegrini, E., et al. 2017, ApJ, 845, 96
D'Agostino, J. J., Kewley, L. J., Groves, B., et al. 2019, ApJ, 878, 2
De Looze, I., Cormier, D., Lebouteiller, V., et al. 2014, A&A, 568, A62
Erb, D. K., Berg, D. A., Auger, M. W., et al. 2019, ApJ, 884, 7
Faisst, A. L., Schaerer, D., Lemaux, B. C., et al. 2020, ApJS, 247, 61
Ferrara, A., Vallini, L., Pallottini, A., et al. 2019, MNRAS, 489, 1
Fujimoto, S., Ouchi, M., Ono, Y., et al. 2016, ApJS, 222, 1
Geach, J. E., Simpson, C., Rawlings, S., Read, A. M., & Watson, M. 2007, MNRAS, 381, 1369
Gong, Y., Cooray, A., Silva, M., et al. 2012, ApJ, 745, 49
González-López, J., Novak, M., Decarli, R., et al. 2020, ApJ, 897, 91
Groves, B. A., & Allen, M. G. 2010, NewA, 15, 614
Harikane, Yuichi, Ouchi, Masami, Inoue, Akio K., et al. 2020, ApJ, 896, 93
Harikane, Y., Ouchi, M., Shibuya, T., et al. 2018, ApJ, 859, 84
Herrera-Camus, R., Bolatto, A. D., Wolfire, M. G., et al. 2015, ApJ, 800, 1
Hodge, J. A., & da Cunha, E. 2020, RSOS, 7, 200556
Hollenbach, D. J., & Tielens, A. G. G. M. 1997, ARA&A, 35, 179
Hunt, L. K., García-Burillo, S., Casasola, V., et al. 2015, A&A, 583, A114
Jaskot, A. E., & Ravindranath, S. 2016, ApJ, 833, 136
Katz, H., Kimm, T., Sijacki, D., & Haehnelt, M. G. 2017, MNRAS, 468, 4831
Kewley, L. J., Nicholls, D. C., & Sutherland, R. S. 2019, ARA&A, 57, 511
Knudsen, K. K., Richard, J., Kneib, J.-P., et al. 2016, MNRAS, 462, L6
Lagache, G., Cousin, M., & Chatzikos, M. 2018, A&A, 609, A130
Langan, I., Ceverino, D., & Finlator, K. 2020, MNRAS, 494, 1988
Langer, W. D., & Pineda, J. L. 2015, A&A, 580, A5
Le Fèvre, O., Béthermin, M., Faisst, A., et al. 2020, A&A, 643, A1
Lebouteiller, V., Péquignot, D., Cormier, D., et al. 2017, A&A, 602, A45
Leitherer, C., Ortiz Otálvaro, P. A., Bresolin, F., et al. 2010, ApJS, 189, 309
Leitherer, C., Schaerer, D., Goldader, J. D., et al. 1999, ApJS, 123, 3
Levesque, E. M., Leitherer, C., Ekstrom, S., Meynet, G., & Schaerer, D. 2012, ApJ, 751, 67
Lupi, A., & Bovino, S. 2020, MNRAS, 492, 2818
Madden, S. C., Cormier, D., Hony, S., et al. 2020, A&A, 643, A141
Madden, S. C., Rémy-Ruyer, A., Galametz, M., et al. 2013, PASP, 125, 600
Maiolino, R., Carniani, S., Fontana, A., et al. 2015, MNRAS, 452, 54
Maiolino, R., Cox, P., Caselli, P., et al. 2005, A&A, 440, L51
Maseda, M. V., van der Wel, A., da Cunha, E., et al. 2013, ApJL, 778, L22
Maseda, M. V., van der Wel, A., Rix, H.-W., et al. 2014, ApJ, 791, 17
Maseda, M. V., van der Wel, A., Rix, H.-W., et al. 2018, ApJ, 854, 29
Masters, D., McCarthy, P., Siana, B., et al. 2014, ApJ, 785, 153
Matthee, J., Sobral, D., Boogaard, L. A., et al. 2019, ApJ, 881, 124
McMullin, J. P., Waters, B., Schiebel, D., Young, W., & Golap, K. 2007, in ASP Conf. Ser. 376, Astronomical Data Analysis Software and Systems XVI, ed. A. Richard et al. (San Francisco, CA: ASP), 127
Olsen, K., Greve, T. R., Narayanan, D., et al. 2017, ApJ, 846, 105
Olsen, K., Greve, T. R., Narayanan, D., et al. 2018, ApJ, 857, 148
Oteo, I., Zwaan, M. A., Ivison, R. J., Smail, I., & Biggs, A. D. 2016, ApJ, 822, 36
Pallottini, A., Ferrara, A., Decataldo, D., et al. 2019, MNRAS, 487, 1689
Planck Collaboration, Aghanim, N., Akrami, Y., et al. 2020, A&A, 641, A6
Plat, A., Charlot, S., Bruzual, G., et al. 2019, MNRAS, 490, 978
Robertson, B. E., Ellis, R. S., Dunlop, J. S., McLure, R. J., & Stark, D. P. 2010, Natur, 468, 49
Robertson, B. E., Ellis, R. S., Furlanetto, S. R., & Dunlop, J. S. 2015, ApJL, 802, L19
Rybak, M. 2017, PhD thesis, Ludwig Maximilian Univ. Munich
Rybak, M., McKean, J. P., Vegetti, S., Andreani, P., & White, S. D. M. 2015, MNRAS, 451, L40
Schaerer, D., Boone, F., Jones, T., et al. 2015, A&A, 576, L2
Schaerer, D., Fragos, T., & Izotov, Y. I. 2019, A&A, 622, L10
Schaerer, D., Ginolfi, M., Béthermin, M., et al. 2020, A&A, 643, A3
Schruba, A., Leroy, A. K., Walter, F., et al. 2012, AJ, 143, 138
Shi, Y., Wang, J., Zhang, Z.-Y., et al. 2016, NatCo, 7, 13789
Silva, M., Santos, M. G., Cooray, A., & Gong, Y. 2015, ApJ, 806, 209
Stacey, G. J., Aravena, M., Basu, K., et al. 2018, Proc. SPIE, 10700, 107001M
Stacey, G. J., Hailey-Dunsheath, S., Ferkinhoff, C., et al. 2010, ApJ, 724, 957
Stark, D. P. 2016, ARA&A, 54, 761
Stark, D. P., Ellis, R. S., Charlot, S., et al. 2017, MNRAS, 464, 469
Stark, D. P., Richard, J., Charlot, S., et al. 2015, MNRAS, 450, 1846
Sutter, J., Dale, D. A., Croxall, K. V., et al. 2019, ApJ, 886, 60
Tang, M., Stark, D. P., Chevallard, J., & Charlot, S. 2019, MNRAS, 489, 2572
Tu, H., Gavazzi, R., Limousin, M., et al. 2009, A&A, 501, 475
Vallini, L., Ferrara, A., Pallottini, A., Carniani, S., & Gallerani, S. 2020, MNRAS, 495, L22
Vallini, L., Ferrara, A., Pallottini, A., & Gallerani, S. 2017, MNRAS, 467, 1300
Vallini, L., Gallerani, S., Ferrara, A., Pallottini, A., & Yue, B. 2015, ApJ, 813, 36
van der Wel, A., Straughn, A. N., Rix, H. W., et al. 2011, ApJ, 742, 111
Verhamme, A., Orlitová, I., Schaerer, D., et al. 2017, A&A, 597, A13
Walter, F., Decarli, R., Aravena, M., et al. 2016, ApJ, 833, 67
Wright, E. L. 2006, PASP, 118, 1711
Yue, B., & Ferrara, A. 2019, MNRAS, 490, 1928
Zanella, A., Daddi, E., Magdis, G., et al. 2018, MNRAS, 481, 1976
Zitrin, A., Ellis, R. S., Belli, S., & Stark, D. P. 2015, ApJL, 805, L7